JOURNAL OF COMPUTATIONAL PHYSICS 49, 490–522 (1983)

Steady Viscous Flows by Compact Differences in Boundary-Fitted Coordinates

XAVIER AUBERT AND MICHEL DEVILLE

Unité de Mécanique Appliquée, Université Catholique de Louvain, Place du Levant, 2, B-1348 Louvain-La-Neuve, Belgium

Received February 11, 1981; revised July 7, 1982

Fourth-order compact differencing is applied to the steady solution of two-dimensional viscous incompressible flows at moderate Reynolds number. The physical region where the fluid flow occurs is mapped onto a rectangle by means of the boundary-fitted coordinates transformation method. The design of the general numerical algorithm rests upon discretization of velocity components and pressure field at the same grid points. The validity of this procedure is assessed by the investigation of a Stokes test problem. Fourth-order numerical results are compared to the analytical solution, second-order results and Chebyshev tau approximation. It is shown that fourth-order differences provide good precision, particularly when the ability of generating irregular meshes is fully exploited. Standard problems as Poiseuille and Couette flows, and the square cavity problem are solved. The fourth-order results on coarse mesh compare favourably with other techniques such as finite element method and second-order differences. A global convergence analysis was performed. On a two-dimensional problem with smooth boundary conditions, one observes a rate of convergence of order four for the velocity components and of order three for the pressure. For the square cavity problem with the two corner singularities, the rates of convergence are decreased by almost an order of magnitude. The solution of a plane constricted channel flow enhances the overall improvement in accuracy, gained by the treatment of the geometrically complex region through the mapping technique.

1. INTRODUCTION

The numerical solution of the Navier–Stokes equations for a viscous fluid flow problem in the presence of a free surface represents one of the most challenging tasks in fluid dynamics. The problem complexity arises from the geometrically complicated form of the domain and from the fact that the surface shape is itself part of the solution of the proposed problem.

In order to avoid the weight of cumulative difficulties, it was decided to treat first the problem of geometric complexity by the elaboration of a numerical algorithm with sufficient generality and precision to allow its application later on to free surface flows.

The aim of this paper is therefore the numerical study of steady state confined flows in complex geometries, bearing in mind the ability of treating free surfaces which will be considered elsewhere. Although finite element techniques seem to be the

0021-9991/83 $3.00

adequate choice for intricated configuration, it is opted for a finite difference approach coupled with a transformation method mapping the physical region onto a rectangle.

Since, in the long run, the calculation algorithm should be able to solve free surface flows, and since the normal-stress boundary condition calls for the pressure knowledge, the velocity components and the pressure are chosen as primary variables.

Previous numerical techniques for viscous-free surface flows with the velocity-pressure formulation used a staggered mesh, where the pressure is cell-centered, while the velocity components are discretized on the cell boundaries (see, e.g., the MAC method [1]). In practice, the pressure is hardly applied at the right surface position and this inaccuracy may lead to meaningless results in a long term integration. Several improvements have been proposed [2]; however, these algorithms present a lack of flexibility to tackle any general form of integration domain.

In this study, the numerical values of the pressure field and velocity components are defined at the same grid nodes. This type of variable placing offers the greatest flexibility for the free surface conditions. Furthermore, with this kind of discretization, the transformation method proposed by Thompson *et al.* [3] allows for an easy mapping of the physical domain on a uniform rectangle, where the numerical integration is carried out. The mapping technique is called the boundary-fitted coordinates system. It can also be viewed as a useful tool for generating nonuniform meshes in regular domains. We *insist* that the present research was carried out in order to solve free surface flows with surface tension at moderate Reynolds number. The placing of the pressure and velocity field at the same point eases the fulfillment of the free surface boundary conditions, as the free surface is mapped onto a coordinate line in the transformed plane.

High Reynolds number flows were not considered in this study. However, the results obtained for moderate values (0 to 100) of the Reynolds number show that the method seems to be promising for that category of flows.

Section 2 describes briefly the basic 2-D equations. Various numerical methods for the solution of the transformed equations are reviewed when the numerical techniques belong to the finite difference approximations with the velocity and pressure defined at the same grid node. In this context, fourth-order compact differences offer an undeniable interest. Section 3 discusses in detail a test problem issued from the Stokes equations solved by variable separation. The model equations written in velocity-pressure variables are treated by second-order finite differences, fourth-order compact differences and Chebyshev tau approximation. Furthermore, the fourth-order compact formulation is coupled with the boundary-fitted coordinates system. The relative merits of each technique are considered. It is shown that although the Chebyshev method achieves the best accuracy, the fourth-order scheme with the mapping procedure constitutes a competitive algorithm which may lead to errors close to those produced by the Chebyshev approximation. Section 4 presents the ADI procedure of the general two-dimensional algorithm. The Poiseuille and Couette flows are solved with the use of the mapping either to produce nonuniform meshes or to generate a

regular region. The resulting errors are small and indicate the excellent global accuracy. In Section 5, the well-known square cavity problem is treated by the fourth-order method with constant and nonuniform mesh sizes. The particular treatment of the pressure singularities at two upper corners of the cavity did not give rise to oscillations propagation and did not compromise the good accuracy of the global solution. The results are in good agreement with those produced by other numerical techniques related to finite difference and finite element methods. One observes that the high accuracy of the scheme together with the ability of constructing nonuniform grids leads to excellent precision with a coarse discretization net. Moreover, a regularized cavity problem with a smooth u velocity distribution on the upper plate has been solved. The rate of convergence for this regular case is of order four for the velocity components and of order three for the pressure. By contrast, the standard cavity presents rates of convergence lowered by almost an order of magnitude. Finally, Section 6 demonstrates the feasibility of the general algorithm by the solution of a constricted plane Poiseuille flow at moderate Reynolds number for various contraction parameters.

From the previous results, one may conclude that the use of a fourth-order accurate difference scheme, coupled with the capability of designing irregular meshes in the regions of interest, leads to the elaboration of an efficient algorithm with the velocity-pressure formulation.

2. The Basic 2-D Equations: Review of Some Velocity-Pressure Algorithms

The physical domain $D(x, y)$ of the flow is transformed into a rectangle $R(\xi, \eta)$ in such a way that each boundary coïncides with a coordinate line ξ or $\eta =$ constant (Fig. 1). The reader is refered to the Appendix for the theoretical background of the mapping technique together with the essential formulas.

The basic equations are the Navier–Stokes and continuity equations which are written in Cartesian coordinates (x, y) of the physical domain. Through the mapping, they are transformed in terms of the (ξ, η) coordinates of the rectangle $R(\xi, \eta)$ and become,

$$-u(y_\eta u_\xi - y_\xi u_\eta)/J - v(-x_\eta u_\xi + x_\xi u_\eta)/J - (y_\eta p_\xi - y_\xi p_\eta)/J + \mathrm{Re}^{-1}[(\alpha u_{\xi\xi} - 2\beta u_{\xi\eta} + \gamma u_{\eta\eta})/J^2 + Pu_\xi + Qu_\eta] = 0, \tag{1}$$

$$-u(y_\eta v_\xi - y_\xi v_\eta)/J - v(-x_\eta v_\xi + x_\xi v_\eta)/J - (-x_\eta p_\xi + x_\xi p_\eta)/J + \mathrm{Re}^{-1}[(\alpha v_{\xi\xi} - 2\beta v_{\xi\eta} + \gamma v_{\eta\eta})/J^2 + Pv_\xi + Qv_\eta] = 0, \tag{2}$$

$$[(y_\eta u)_\xi - (y_\xi u)_\eta + (x_\xi v)_\eta - (x_\eta v)_\xi]/J = 0. \tag{3}$$

In (1)–(3), u and v are the Cartesian velocity components in the physical plane, p denotes the pressure, Re is the Reynolds number, and $[x_\xi, x_\eta, y_\xi, y_\eta, J, \alpha, \beta, \gamma, P, Q]$

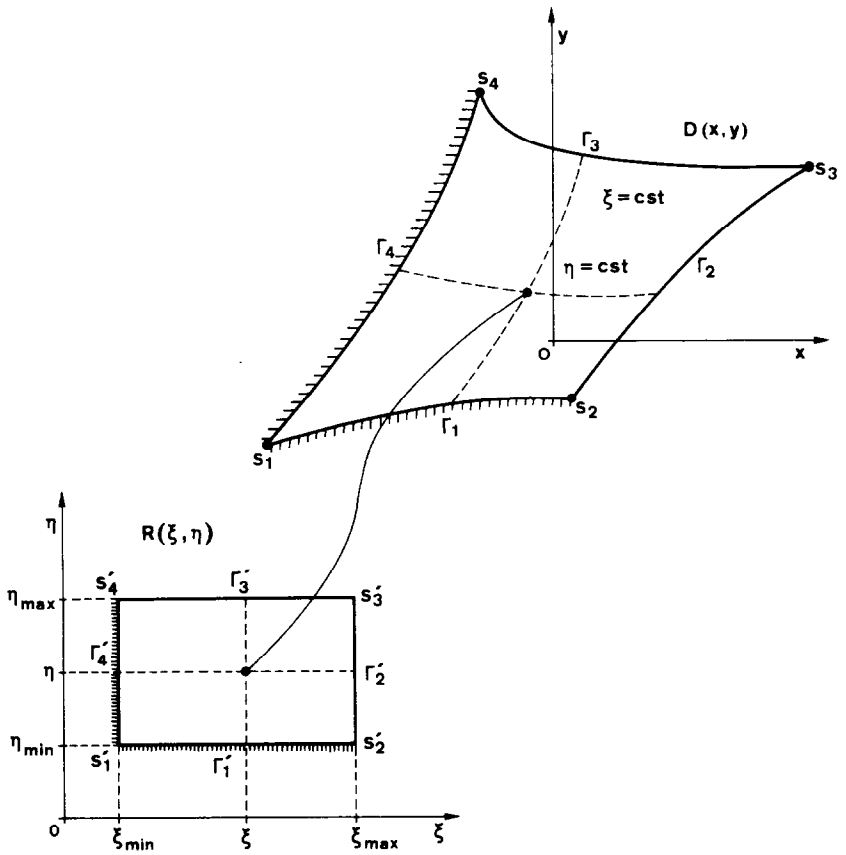

FIG. 1. Mapping of the physical domain on a rectangle.

are the geometrical coefficients associated with the transformation. It should be noted that the divergence operator in continuity equation (3) is written in conservative form.

Standard centered finite difference operators of second-order accuracy can be used to solve numerically the Navier–Stokes equations (1) and (2), with the natural coordinates. This research was accomplished by Hodge [4] and Thompson [5] for transient problems by means of a computational algorithm coupling an interior Poisson's equation for the pressure and the artificial compressibility technique due to Chorin [6] on the boundaries.

The artificial compressibility technique uses an evolutionary equation

$$p^{(s+1)} = p^{(s)} - c^2 \operatorname{div} \mathbf{v}, \tag{4}$$

where $c^2 > 0$, $\mathbf{v}$ is the vector notation for the velocity field, and s is an iteration counter. Equation (4) is applied to each discretization point.

The previous procedure proposed by Thompson (interior Poisson's equation and artificial compressibility at the walls) is needed because the application of (4) to the complete computational domain leads to unbearable oscillations in the pressure field. These oscillations come from the second-order centered finite differencing of the div v operator, which is written on a regular grid of mesh size h as the following relation:

$$(\text{div } \mathbf{v})_{i,j} \simeq \frac{u_{i+1,j} - u_{i-1,j}}{2h} + \frac{v_{i,j+1} - v_{i,j-1}}{2h} + O(h^2).$$

This formula clearly shows the uncoupling of the discrete velocities in two independent and intertwined subgrids. Therefore, the pressure computation by Eq. (4) at each discretization point leads to oscillations of period $2h$. This is the reason why Thompson [5] treats a Poisson's equation for the internal pressure with Dirichlet boundary conditions provided by the artificial compressibility scheme (4). However, this procedure may generate velocity fields which are not divergence-free, particularly in the neighbourhood of the walls. This difficulty to satisfy the incompressibility constraint has a straightforward explanation, when one notices that the discrete Poisson's equation is not strictly equivalent to the equation div $\mathbf{v} = 0$. As a matter of fact, the discrete second-order centered operators do not verify the identity

$$\nabla^2 = \text{div}(\text{grad})$$

and therefore, the Poisson's equation does not lead necessarily to a rigorous mass conservation. These convergence difficulties and the poor precision of the results obtained by this algorithm led the present authors to fourth-order compact differences, while retaining the placing of the velocity components and the pressure at the same node. This last element constitutes to our point of view an essential feature to solve a free surface flow properly. The compact operators are characterized by an implicit relation between the function values and its derivatives at three consecutive points. The implicitness of the operator avoids the uncoupling of the velocities on the grid. Furthermore, fourth-order compact operators provide an improved accuracy. As a consequence, all the reported computations were performed, on a mini-computer with discrete meshes of moderate size, but for the 31×31 and 41×41 computations in the convergence analysis which were run on an IBM 370/158 computer.

As the behaviour of the pressure-velocity formulation with discretized variables attached to the same nodes has been seldom studied, the next section investigates the accuracy of several finite difference schemes and of the Chebyshev spectral method on a test problem designed and solved with the above assumptions. The emphasis of the test bears on the incompressibility condition and not on the nonlinearity of the Navier–Stokes operator.

3. Test Problem

Incompressible fluid dynamics is very much dependent on the way the divergence-free constraint on the velocity field is enforced. To discriminate how the spatial resolution through the numerical approximation affects the calculation, a steady version of a test problem proposed by Gottlieb and Orszag [7] has been devised.

Let us assume variable separability and suppose that the Stokes equations (vanishing Reynolds number) are solved within the slab $0 \leqslant x \leqslant 1$, $-\infty \leqslant y \leqslant \infty$. The velocity components and the pressure field may be written as,

$$\mathbf{v} = (u(x)\, e^{iky}, v(x)\, e^{iky}), \qquad p = p(x)\, e^{iky}. \tag{5}$$

The steady Stokes equations with a forcing term of magnitude one reduce to a problem depending only on the x coordinate,

$$-p_x + \nu(u_{xx} - k^2 u) + 1 = 0, \tag{6a}$$

$$-ikp + \nu(v_{xx} - k^2 v) = 0, \tag{6b}$$

$$u_x + ikv = 0, \tag{6c}$$

subject to the no-slip boundary conditions $\mathbf{v}(0) = \mathbf{v}(1) = 0$. In Eqs. (6), p denotes the pressure divided by the constant density and ν is the kinematic viscosity.

The vertical velocity component can be expressed in terms of u by continuity equation (6c) and the pressure can be eliminated between (6a) and (6b). The problem described by Eqs. (6) is therefore reduced to a single fourth-order differential equation in u,

$$\left(\frac{d^2}{dx^2} - k^2\right)^2 u = \frac{k^2}{\nu}. \tag{7}$$

The boundary conditions are now

$$u(0) = u(1) = u_x(0) = u_x(1) = 0.$$

The analytical solution of (7) can be written as

$$k^2 \nu u(x) = 1 - \cosh kx + [(\cosh k - 1)(\sinh kx - kx \cosh kx) + kx \sinh k \sinh kx]/(\sinh k + k). \tag{8}$$

The model problem described by Eqs. (6) has been solved by several numerical techniques: second-order finite differences, fourth-order compact differences, and Chebyshev spectral methods. In every approximation, the u, v, p variables are discretized at the *same* nodes.

For second-order finite differencing, classical second-order centered operators were used. For fourth-order compact differencing, Kreiss' scheme (Orszag and Israeli [8],

Hirsh [9]) has been considered. In the latter method, the first- and second-order derivatives of a function f are approximated by

$$f'_i = \{D_0/(1 + \tfrac{1}{6}h^2 D_+ D_-)\} f_i, \tag{9}$$

$$f''_i = \{D_+ D_-/(1 + (1/12)\, h^2 D_+ D_-)\} f_i, \tag{10}$$

where $D_0 f_i = (1/2h)(f_{i+1} - f_{i-1})$, $D_+ f_i = (1/h)(f_{i+1} - f_i)$, and $D_- f_i = (1/h)(f_i - f_{i-1})$. Denoting the new unknowns $F_i = f'_i$ and $S_i = f''_i$, the two previous equations (9) and (10) lead to the equivalent tridiagonal relationships,

$$\tfrac{1}{6}(F_{i+1} + 4F_i + F_{i-1}) = (1/2h)(f_{i+1} - f_{i-1}), \tag{11}$$

$$\tfrac{1}{12}(S_{i+1} + 10S_i + S_{i-1}) = (1/h^2)(f_{i+1} - 2f_i + f_{i-1}). \tag{12}$$

Note that the previous relationships are typical of fourth-order compact operators and induce an implicit relation between neighbouring function values and its derivatives.

To solve tridiagonal equations (11) and (12) from a given set of f_i ($1 \leqslant i \leqslant N + 1$; N is the number of intervals), the algebraic system must be closed by boundary conditions preserving the tridiagonal character. Equation (13) called the second diagonal Padé approximant, fulfills this condition:

$$f_i - f_{i+1} + (h/2)(F_i + F_{i+1}) + (h^2/12)(S_i - S_{i+1}) + O(h^5) = 0. \tag{13}$$

Let us observe that second-order and fourth-order compact differences for the first- and second-order derivatives can be cast into a general tridiagonal formulation,

$$aF_{i+1} + bF_i + aF_{i-1} = (1/2h)(f_{i+1} - f_{i-1}), \tag{14}$$

$$cS_{i+1} + dS_i + cS_{i-1} = (1/h^2)(f_{i+1} - 2f_i + f_{i-1}). \tag{15}$$

For $a = c = 0$ and $b = d = 1$, second-order differencing is recovered, while for $a = \frac{1}{6}$, $b = \frac{2}{3}$, $c = \frac{1}{12}$, and $d = \frac{5}{6}$, fourth-order compact differences are regained.

With the above remark in mind and using the previous definitions, for an internal discretization point ($2 \leqslant j \leqslant N$), the algebraic system takes the form,

$$p'_j + \nu(k^2 u_j - u''_j) = 1, \tag{16a}$$

$$ikp_j + \nu(k^2 v_j - v''_j) = 0, \tag{16b}$$

$$-ik(av_{j+1} + bv_j + av_{j-1}) = (1/2h)(u_{j+1} - u_{j-1}), \tag{16c}$$

$$ap'_{j+1} + bp'_j + ap'_{j-1} = (1/2h)(p_{j+1} - p_{j-1}), \tag{16d}$$

$$cu''_{j+1} + du''_j + cu''_{j-1} = (1/h^2)(u_{j+1} - 2u_j + u_{j-1}), \tag{16e}$$

$$cv''_{j+1} + dv''_j + cv''_{j-1} = (1/h^2)(v_{j+1} - 2v_j + v_{j-1}). \tag{16f}$$

Equations (16a) and (16b) are the Stokes equations. Equation (16c) is obtained from (11) applied to u_j' and combined to the continuity equation.

At the boundary (node 1, for example), the equations are

$$\begin{aligned} u_1 = v_1 = 0, \\ u_1 - u_2 - \frac{hk}{2}(v_1 + v_2) + (h^2/12)(u_1'' - u_2'') = 0, \\ p_1' - \nu u_1'' = 1, \\ ikp_1 - \nu v_1'' = 0, \\ (p_1 - p_2)(1 + h^2k^2/12) + (h/2)(p_1 + p_2) = 0. \end{aligned} \tag{17}$$

The last equation of (17) is obtained from Padé relation (13) applied to the first grid point and by replacing the second-order derivative p_{xx} by k^2p as for a Stokes flow, the pressure is a harmonic function.

From (16) and (17), it can be seen that the complete algebraic system presents a block-tridiagonal structure, where the blocks are of order six. This system can be solved by a direct standard LU factorization (see for example, Isaacson and Keller [10]). The direct solution is made possible because of the variable separability, which allows a nonsingular pressure calculation.

For $\nu = 10^{-2}$ and $k = 4$, Fig. 2a displays the behaviour of the dependent variables. Table I shows the relative error on the horizontal velocity component u at $x = 0.1$ and 0.5 and the relative error on the pressure at $x = 0.0$ and 0.4 for second- and fourth-order approximations and different values of the interval number. The computed divergence is at the level of the computer round-off error.

The Chebyshev spectral method assumes that the dependent variables may be represented in terms of particular orthogonal polynomials, namely,

$$\begin{aligned} u(x) = \sum_{n=0}^{N} u_n T_n(2x-1), \qquad v(x) = \sum_{n=0}^{N} v_n T_n(2x-1), \\ p = \sum_{n=0}^{N} p_n T_n(2x-1), \qquad 0 \leqslant x \leqslant 1, \end{aligned} \tag{18}$$

where $T_n(2x-1)$ is the nth-order Chebyshev polynomial of the first kind. The discrete equations are obtained by the tau approximation (Gottlieb and Orszag [7]),

$$\begin{aligned} p_n^{(1)} + \nu(k^2 u_n - u_n^{(2)}) = \delta_{0,n}, \qquad 0 \leqslant n \leqslant N-2, \\ ikp_n + \nu(k^2 v_n - v_n^{(2)}) = 0, \qquad 0 \leqslant n \leqslant N-2, \\ u_n^{(1)} + ikv_n = 0, \qquad 0 \leqslant n \leqslant N, \\ \sum_{n=0}^{N} u_n = \sum_{n=0}^{N} (-1)^n u_n = \sum_{n=0}^{N} v_n = \sum_{n=0}^{N} (-1)^n v_n = 0, \end{aligned} \tag{19}$$

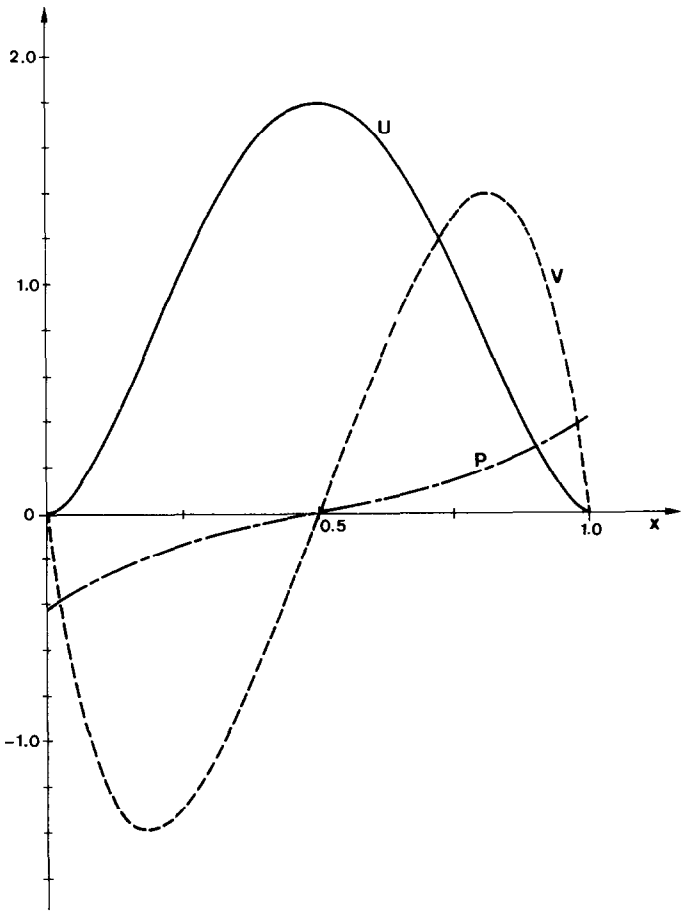

FIG. 2a. Analytical solution for the Stokes test problem: $v = 10^{-2}$, $k = 4$.

where $\delta_{0,n}$ is the Kronecker symbol and

$f^{(i)}$ denotes the ith-order derivative of f in terms of the original shifted Chebyshev polynomials.

If $f(x) = \sum_{n=0}^{N} f_n T_n(2x-1)$, then

$$\frac{df}{dx} = \sum_{n=0}^{N} f_n^{(1)} T_n(2x-1), \qquad f_n^{(1)} = \frac{4}{c_n} \sum_{\substack{p=n+1 \\ p+n \text{ odd}}}^{N} p f_p,$$

$$\frac{d^2 f}{dx^2} = \sum_{n=0}^{N} f_n^{(2)} T_n(2x-1), \qquad f_n^{(2)} = \frac{2}{c_n} \sum_{\substack{p=n+2 \\ p+n \text{ even}}}^{N} p(p^2-n^2) f_p.$$

In these relations, $c_0 = 2$ and $c_n = 1$ for $n > 0$.

TABLE I

Relative Error on u and p at Fixed Points Inside the [0, 1] Interval with Respect to the Order of the Finite Difference Scheme and the Number of Intervals ($\nu = 0.01, k = 4$)

N	Order	$u(0.1)$	$u(0.5)$	$p(0.0)$	$p(0.04)$
10	2	2.1(−1)	2.8(−2)	4.0(−2)	1.8(−2)
20	2	5.8(−2)	7.8(−3)	1.1(−2)	5.0(−3)
30	2	2.6(−2)	3.5(−3)	5.4(−3)	2.4(−3)
40	2	1.5(−2)	2.0(−3)	3.0(−3)	1.4(−3)
10	4	1.8(−3)	4.2(−4)	5.4(−4)	3.87(−4)
20	4	1.7(−4)	3.3(−5)	4.2(−5)	2.66(−5)
30	4	3.2(−5)	6.4(−6)	9.0(−6)	5.45(−6)
40	4	1.05(−5)	2.1(−6)	2.95(−6)	1.76(−6)

Note. The numbers between parentheses are the exponents of the scientific notation.

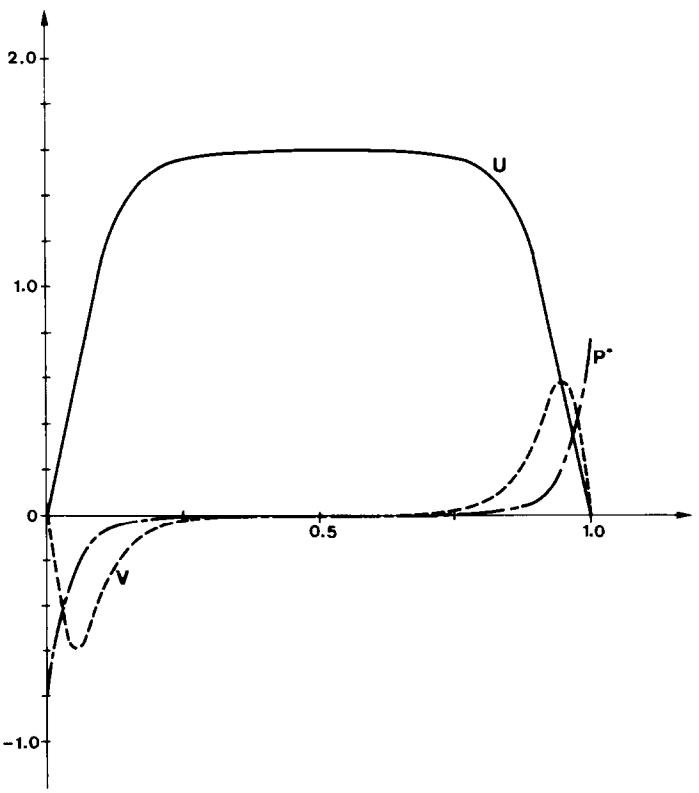

FIG. 2b. Analytical solution for the Stokes test problem: $\nu = 10^{-2}$, $k = 25$ ($p^* = P \times 10$, $P =$ pressure).

It is well known that in absence of singularity, spectral methods offer "infinite" convergence since the error goes to zero faster than any finite power of $1/N$. This assertion is confirmed by the solution of problem (6) through the Chebyshev tau approximation (19) with the same set of parameters as before ($\nu = 10^{-2}$; $k = 4$). For $N = 20$, the maximum relative error on u occurs at the central point and is 3.10^{-14}, while for $N = 10$, the maximum relative error is $9.6\ 10^{-7}$. A relative error of $5.2\ 10^{-5}$ is obtained for $N = 8$. This error is of the same order of magnitude as that produced by a fourth-order compact method with 20 intervals. Therefore, one can conclude that for the same achieved accuracy, fourth-order differences need at least twice as many degrees of freedom as spectral methods.

As pointed out in the previous section, boundary-fitted coordinates can take the geometric complexity into account and control easily the internal mesh distribution to result in a better discretization grid. This last property can prove very interesting in regions where high gradients occur. We will compare in the remainder of this section the solution of problem (6) with $\nu = 10^{-2}$ and $k = 25$ by the Chebyshev tau projection method and the fourth-order compact differencing coupled with Thompson's mapping. The exact solution for u with $k = 25$ presents a boundary layer-type behaviour near the limits, while the velocity profile is almost flat over a large part of the unit interval. (Fig. 2b).

Using the fourth-order compact formulation, the one-dimensional natural coordinates, and with the help of (A9), it is easy to show that the Stokes problem (16) resumes a block tridiagonal form.

Figure 3 shows the comparison of several grids generated by (A7) with different values of a_i in Eq. (A8). The number of intervals remains constant and is equal to 20. For the sake of comparison, the last grid corresponds to the Chebyshev abscissas in conjunction with the tau method. The finite difference mesh may be equally spaced or nonuniformly distributed. In case of a variable mesh, the mapping results from a fourth-order accurate computation. Figure 3 also presents the maximum relative error on u for the various computations. One notices that the grid points definition influences the results deeply, and the maximum relative error decreases by a factor of 43 between the calculation on a regular mesh and that carried out on the unequally spaced grid characterized by the parameters $a_i = 350$, $c_i = 0.1$.

We may notice that it is always better to refine the grid in regions of high gradients. The precision gain is always noticeable with respect to results obtained on an equipartitioned grid.

Finally, a convergence analysis was carried out on this problem for the determination of the effective rate of convergence. Both cases ($\nu = 10^{-2}$, $k = 4$ and 25) solved Eqs. (16) and (17) on equidistant grids with $N = 10$, 20, 30, 40 and with the help of standard second-order operators and 4th-order compact operators, respectively. For each discretization, L_2 absolute errors are evaluated for u, v, p with respect to the analytical solution (8). The results are reported on log–log diagrams. Figure 2c corresponds to the case $k = 4$ while Fig. 2d presents the test $k = 25$.

With the different operators (2nd or 4th order), the first test has a rate of convergence of 2.37 and 4.4, respectively, for u, v, p, while the second problem

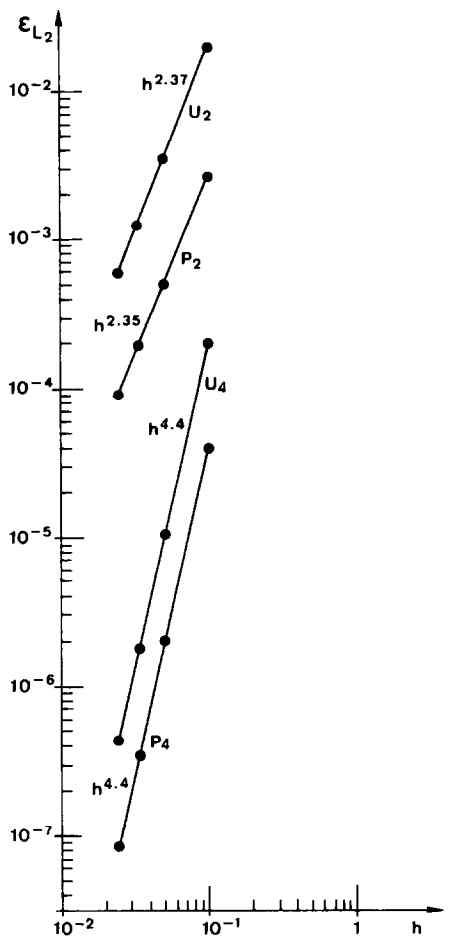

FIG. 2c. Log–log error plot of u and p for the case: $\nu = 10^{-2}$, $k = 4$.

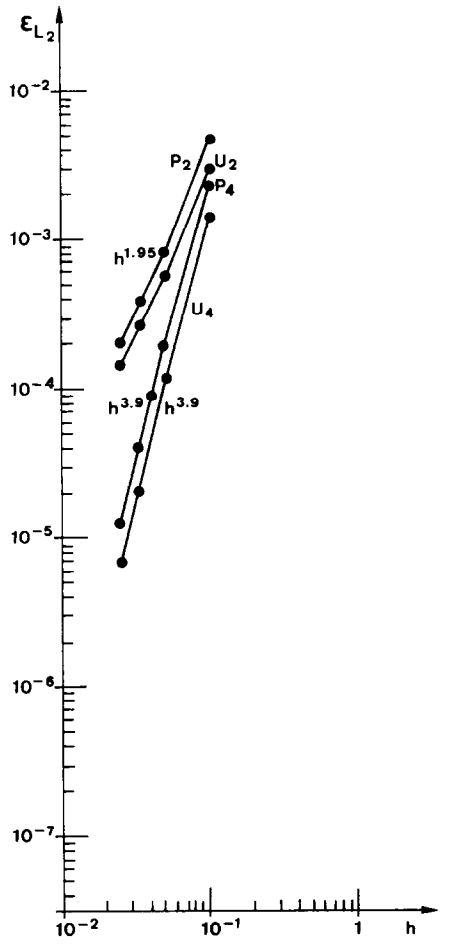

FIG. 2d. Log–log error plot of u and p for the case: $\nu = 10^{-2}$, $k = 25$.

reveals a u, v, p convergence of 1.95 and 3.9 for the finest grids. These numerical results confirm the theoretical rates of convergence. The compact operators provide errors at levels of several orders of magnitude less than those produced by standard finite difference formulas for an equal number of degrees of freedom.

The computed results in this section show that the Chebyshev method offers the best accuracy as Chebyshev polynomials satisfy a minimax property in the interpolation theory. However, fourth-order compact differences coupled with the boundary-fitted coordinates are very superior to the classical second-order differences on uniform meshes, as far as attainable precision and geometric versatility are concerned. These are essentially the reasons why the next sections present a numerical method for viscous flow by compact differences on boundary-fitted coordinates.

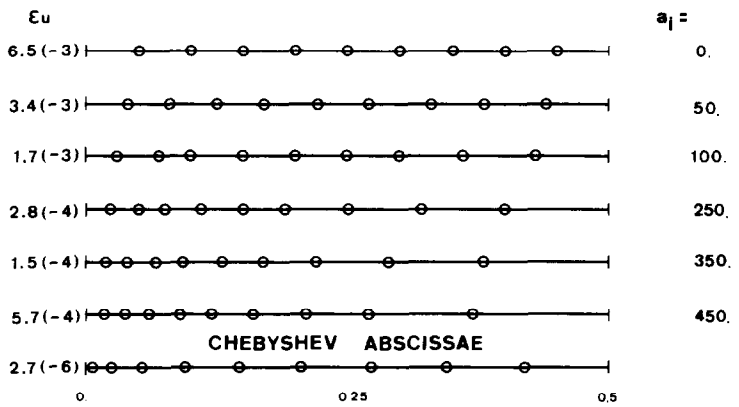

FIG. 3. Maximum relative error on u for fourth-order calculations and Chebyshev tau approximation.

4. General Two-Dimensional Algorithm and Numerical Accuracy

As explained in Section 2, the two-dimensional domain $D(x, y)$ is transformed into a rectangle $R(\xi, \eta)$, where the numerical integration of the steady Navier–Stokes equations is performed. The rectangular form of the mapped domain comes from a particular choice pertinent to the present study. Other general configurations are possible (see [3, 5]). The discrete grid is characterized by a constant mesh size $h = 1$, and includes $(N+1) \times (M+1)$ nodes covering the whole rectangle $R(\xi, \eta)$ $(1 \leqslant \xi \leqslant N+1,\ 1 \leqslant \eta \leqslant M+1)$.

The governing equations are (1)–(3). The basic boundary conditions are given u and v velocity components on the limits of $D(x, y)$, which are compatible with the mass flow rate conservation.

In two dimensions, the computation of the pressure field is no longer as easy as for the test problem solved in Section 3 by a direct imposition of continuity equation (3). Therefore, the continuity constraint is replaced by transient equation (4) which will be equivalent when the convergence is reached (div $\mathbf{v} = 0$). This technique is a coherent procedure with respect to the use of fourth-order compact operators, even though the u, v, p variables are defined at the same nodes. The steady solutions of the previous test problem obtained by using the transient method with Eq. (4) replacing (6c) achieve the same accuracy as observed for the compact direct solution, while the computing time increases due to the iterative character of the process. This result confirms the implicit coupling of the nodes by the 4th-order compact operators and allows the use of scheme (4) for the calculation of 2-D flows without the appearance of spurious pressure oscillations (see Sections 5 and 6).

The general algorithm consists in converting the basic steady-state Navier–Stokes equations (1) and (2) into a transient form by the introduction of partial time

derivatives together with the artificial compressibility method. With this evolutionary form, the false transient algorithm due to Mallinson and De Vahl Davis [11] yields efficiently the steady solution. A classical ADI process is designed.

Let s denote the iteration counter, Δt the time step, c^2 the artificial compressibility parameter, and define auxiliary variables by the expressions,

$$\phi = (y_\eta u - x_\eta v)/J - (P/\mathrm{Re}), \tag{20a}$$

$$\chi = (y_\xi u - x_\xi v)/J - (Q/\mathrm{Re}). \tag{20b}$$

In Eqs. (20), P and Q are given functions regulating the mesh interval inside the domain, (see Appendix). Notice that p will denote the pressure. Hereafter, the equations for the first sweep of the ADI procedure in the ξ direction are collected.

a. *Equations for an Interior Point* (i, j), $(2 \leqslant i \leqslant N,\ 2 \leqslant j \leqslant M)$

$$[u^{s+1}/\Delta t + y_\eta p_\xi^{s+1}/J - \mathrm{Re}^{-1}\, \alpha u_{\xi\xi}^{s+1}/J^2]_{i,j} \tag{21a}$$
$$= [u^s/\Delta t - u_\xi^s \phi^s + u_\eta^s \chi^s + y_\xi p_\eta^s/J + \mathrm{Re}^{-1}(-2\beta u_{\xi\eta}^s + \gamma u_{\eta\eta}^s)/J^2]_{i,j},$$

$$[v^{s+1}/\Delta t - x_\eta p_\xi^{s+1}/J - \mathrm{Re}^{-1}(\alpha v_{\xi\xi}^{s+1} - 2\beta v_{\eta\xi}^{s+1})/J^2]_{i,j}$$
$$= [v^s/\Delta t - v_\xi^s \phi^s + v_\eta^s \chi^s - x_\xi p_\eta^s/J + \mathrm{Re}^{-1}\, \gamma v_{\eta\eta}^s/J^2]_{i,j}, \tag{21b}$$

$$[p^{s+1} + c^2(x_\eta v^{s+1} - y_\eta u^{s+1})_\xi/J]_{i,j} = [p^s - c^2(x_\xi v^s - y_\xi u^s)_\eta/J]_{i,j} \tag{21c}$$

The derivatives u_ξ, v_ξ, p_ξ, $u_{\xi\xi}$, $v_{\xi\xi}$ at an internal point are computed by relationships like (11) or (12) written in the (ξ, η) plane with $\eta = \text{const}$ and $h = 1$.

The mixed derivative $v_{\eta\xi}$ comes from a tridiagonal equation of type (11) applied to $f = v_\eta$ and $F = v_{\eta\xi}$.

b. *Equations for Vertical Walls* $(i = 1 \text{ or } N + 1,\ 2 \leqslant j \leqslant M)$

The u and v velocities are prescribed on the boundaries. The pressure is evaluated by Eq. (21c). The second Padé diagonal approximant (13) supplies adequate expressions for the u_ξ and v_ξ boundary conditions, while the quantities p_ξ and $v_{\eta\xi}$ are obtained by means of a third-order Hermite relation given by Elsaesser and Peyret [12]. For example, on a vertical left wall, one has for the p_ξ computation

$$p_\xi(1, j) + 2p_\xi(2, j) - (1/2h)(-5p(1, j) + 4p(2, j) + p(3, j)) = 0 + O(h^3). \tag{22}$$

For the second-order derivatives, the system of equations is closed by using the corresponding momentum equation on the boundary.

c. *Equations for Horizontal Walls* $(j = 1 \text{ or } M + 1,\ 1 \leqslant i \leqslant N + 1)$

These boundary lines are treated as in Subsections a and b, with u and v prescribed everywhere. The velocity derivatives u_ξ, v_ξ, $u_{\xi\xi}$, $v_{\xi\xi}$ are obtained from u and v

through compact operators. The pressure is again generated by Eq. (4) applied to the boundary.

(i) The algebraic system of the equations describing the ξ sweep has a block-tridiagonal structure where the unknowns are, respectively, u, v, p, u_ξ, v_ξ, p_ξ, $u_{\xi\xi}$, $v_{\xi\xi}$, $v_{\eta\xi}$.

(ii) For the second η sweep, similar equations may be written leading to an analogous block-tridiagonal system, with u, v, p, u_η, v_η, p_η, $u_{\eta\eta}$, $v_{\eta\eta}$, $u_{\xi\eta}$ as unknowns.

(iii) One should note that the algorithm does not require any boundary condition for the pressure and the tangential velocity derivatives to the domain contour. As will be seen in Sections 5 and 6, the treatment of the boundary conditions can be extended easily to a symmetry axis or to natural outflow conditions. Furthermore, the boundary conditions are able to handle problems with discontinuous distribution of boundary velocities. Note that in Eq. (21c), the divergence operator is written under conservative form. This point is essential for cases presenting in- and outflow boundaries to enforce rigorous mass conservation in the flow region.

The convergence of the iterative process is governed by stability criteria, which are derived by a von Neumann stability analysis. Conditions are

$$c^2 > 0, \qquad c^2 \leqslant 2/\mathrm{Re}, \qquad \Delta t \leqslant (\sqrt{3})^{-1} \min_{i,j} (x_\xi(i,j), y_\eta(i,j))/\max_{i,j} (u_{i,j}, v_{i,j}).$$

To test the global numerical accuracy of the proposed algorithm, numerical solutions were devised on Poiseuille and Couette flows, where analytical solutions are available.

Inside the domain $0 \leqslant x, y \leqslant 1$, the *Poiseuille flow* solution is a quadratic solution, $u = y(1-y)$. On a uniform mesh, the fourth-order compact method reproduces the exact solution to within the machine accuracy. However, as soon as the grid is nonuniform and distorted, errors appear from the combined effect of the coordinates transformation and the truncation error on the transformed equations. (Note that in the ξ–η plane, the u velocity component is no longer a quadratic.)

Figure 4 displays for $N = 10$ ($h = 10^{-1}$), a highly distorted grid ($a_i = 250$, $c_i = 1$). In that case, the maximum absolute error on u and p is 7.10^{-6} and 10^{-4}, respectively. These values are quite satisfactory and prove that good overall accuracy is reached.

For the *Couette flow problem*, if one refers to Cartesian coordinates and if the two concentric cylinders are centered at the $(-1, -1)$ point, the theoretical solution has the form,

$$u = -(A + B/F)(1 + y), \qquad v = (A + BF)(1 + x),$$
$$p = A^2/2F + 2AB \log r - B^2F/2 + \text{const}, \qquad p = \text{const}$$

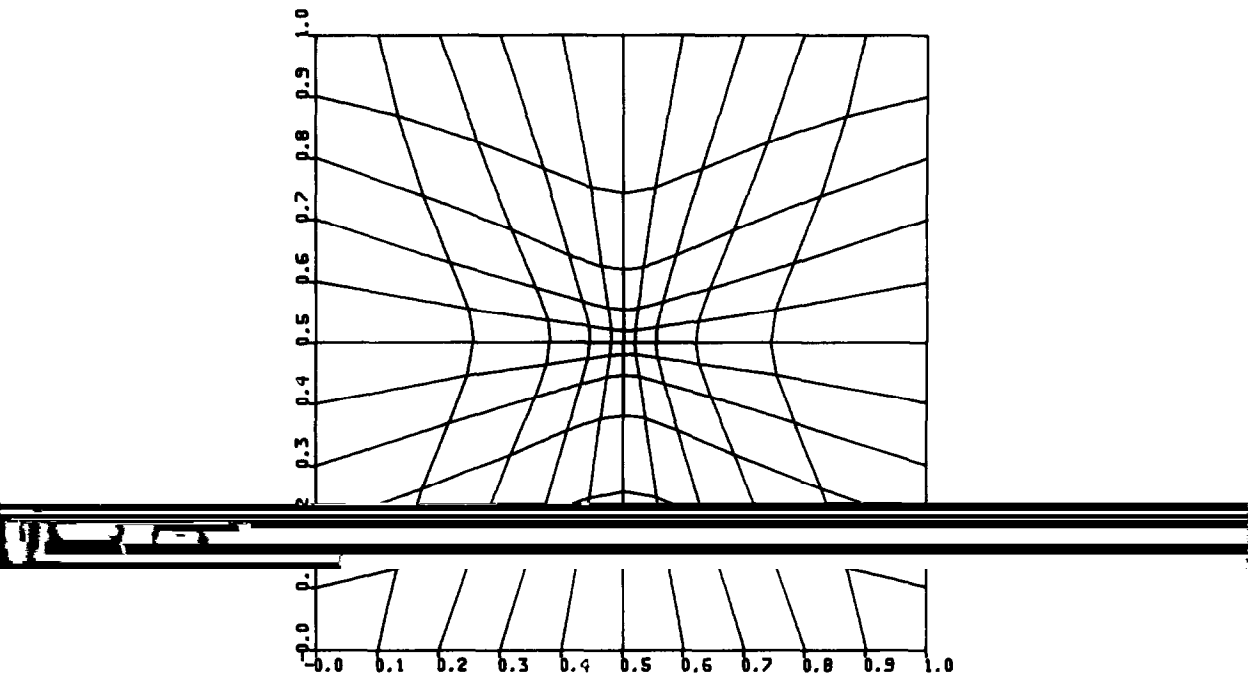

FIG. 4. Highly distorted 10×10 grid for Poiseuille flow.

for Stokes flow, where

$$A = (\Omega_0 R_0^2 - \Omega_i R_i^2)/(R_0^2 - R_i^2),$$
$$B = (\Omega_i - \Omega_0) R_i^2 R_0^2/(R_0^2 - R_i^2), \tag{23}$$
$$r = [(1+x)^2 + (1+y)^2]^{1/2}, \qquad F = 1/r^2.$$

In the previous expressions R_i, R_0, Ω_i, Ω_0 designate the inner and outer radii and the inner and outer rotation velocities of the cylinders, respectively.

The first Couette test is concerned with the flow around the inner cylinder, in an infinite domain ($R_0 = \infty$, $\Omega_0 = 0$). The inner radius is chosen in such a way that $\Omega_i R_i^2 = 2$. The set of parameters in (23) is $A = 0$, $B = 2$. The computational domain is the square $0 \leqslant x, y \leqslant 1$, covered by a grid of $N \times N$ square cells.

The second test problem computes the internal flow between the concentric cylinders centered at $(-1, -1)$. Setting $\Omega_i = 0$, $R_i = 0.5$, $R_0 = \Omega_0 = 1$, the solution is Eq. (23) with $A = \frac{4}{3}$ and $B = -\frac{1}{3}$. The computation is performed in the quarter of an annulus defined by $0.5 \leqslant r \leqslant 1$ and $0 \leqslant \theta \leqslant 90$ (Fig. 5). The mapping transforms the physical region in a regular rectangle where the ξ and $\eta = \text{const}$ lines are the analog of the r and $\theta = \text{const}$ lines.

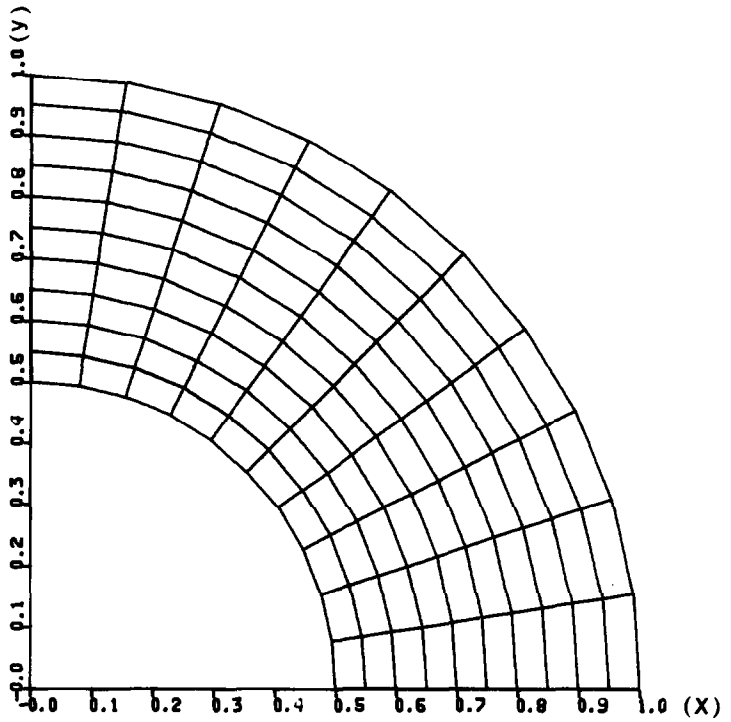

FIG. 5. Discretization grid for Couette flow ($N = 10$, $R_i = 0.5$, $R_0 = 1$).

TABLE II

Maximum Absolute Errors on the Velocity and Pressure Fields in a Couette Flow Solved by Fourth-Order Compact Methods with Constant Mesh Size

Authors	N	Re	ε_u	ε_v	ε_p
Present	10	0	9.0(−7)	9.0(−7)	4.0(−5)
Present	14	100	7.0(−7)	7.0(−7)	6.0(−6)
[12]	10	100	8.0(−6)	9.7(−6)	1.6(−4)
[12]	20	100	7.0(−7)	6.0(−7)	1.4(−5)

Note. N is the number of intervals in each spatial direction and Re represents the flow Reynolds number.

TABLE III

Maximum Absolute Errors of Dependent Variables for a Creeping Couette Flow Solved on a Transformed Quarter of Annulus

N	ε_u	ε_v	ε_p
6	9.0(−6)	9.0(−6)	3.5(−4)
10	1.0(−6)	1.0(−6)	5.0(−5)
12	5.0(−7)	5.0(−7)	2.4(−5)

Both tests are run with the velocity field given on the boundaries. The initial internal guess consists of vanishing pressure and velocity fields.

For the first Couette test, Table II depicts the maximum absolute errors on the velocity components and the boundary pressure for Re (defined as $\Omega_i R_i^2/\nu) = 0$, 100. The present computations compare favourably to those by Elsaesser and Peyret [12] and corroborate their convergence analysis on the same problem, which shows the method achieves fourth-order convergence.

Table III yields the maximum absolute errors on the dependent variables for the second Couette flow, at zero Reynolds number. The small error level confirms obviously the excellent global accuracy of the coordinate transformation for a nontrivial geometric domain. The errors decay with an $O(h^4)$ rate.

5. The Square Cavity Problem

To assess definitively the accuracy of the general algorithm and its feasibility in presence of singularities, the square cavity problem (Fig. 6) is solved by the numerical procedure described in Section 4. However, to take the pressure singularities at the two upper corners into account, we made a particular choice for the boundary conditions which is compatible with the physics of the problem and with the use of fourth-order operators.

In the mathematical continuous problem, the horizontal velocity component u is not univocally defined at the two upper corners. This horizontal component is one on the interior of Γ_4 while it is zero on the other sides, but at the two points ($y = 1$, $x = 0$ and $x = 1$). The vertical component v vanishes on the four walls. To remove the indetermination, we impose $u = 0$ at the two upper corners. This condition ensures $u_y = u_{yy} = 0$ on Γ_1 and Γ_3. Therefore, the u distribution on the upper lid of the cavity is a step function and presents a jump from zero to one in the vicinity of the singularities. The conditions $u_x = u_{xx} = 0$ hold on the interior of Γ_4.

The numerical process is adapted to the particular treatment of the singularities to avoid oscillations propagation in the discontinuities neighbourhood when the u_x and u_{xx} computation on Γ_4 is carried out by fourth-order operators. The discretized problem approaches continuously the step function and is characterized by given

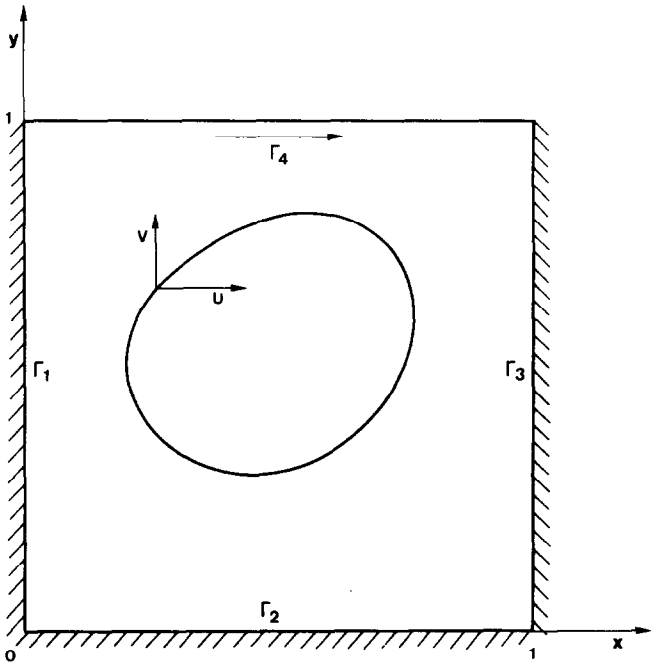

FIG. 6. Square cavity problem.

finite values of u_x and u_{xx} at the two upper corners. For this discrete model, the requirement div $\mathbf{v} = 0$ is demanded at these two points and therefore, $u_x = 0$ as v_y vanishes identically on Γ_1 and Γ_3. The general algorithm of Section 4 allows the possibility of imposing tangential velocity derivatives to the contour. With the previous choice of u distribution on Γ_4, we may require

$$u_x(i, M+1) = u_{xx}(i, M+1) = 0, \qquad 2 \leqslant i \leqslant N.$$

Near the two singularities, the u velocity component is approximated on the first or last interval by Hermite interpolation through a polynomial of degree four. For example, at the left upper corner, we have the following five conditions:

$$u(1, M+1) = 0, \qquad u(2, M+1) = 1, \qquad u_x(1, M+1) = 0,$$
$$u_x(2, M+1) = 0, \qquad u_{xx}(2, M+1) = 0.$$

Padé relation (13) yields the u_{xx} value at the singularity

$$u_{xx}(1, M+1) = 12/h^2.$$

From the computational point of view, the algorithm fulfills the condition $u_x = 0$ at the two upper corners *iteratively* by the artificial compressibility scheme that

generates at the same time the corner pressures. For example, at the upper left corner the pressure is obtained by the next relation (the following equations are written for simplicity in the case of a regular grid with mesh size h and may be generalized to the $\xi - \eta$ formalism)

$$p^{s+1}_{1,M+1} = p^{s}_{1,M+1} - c^2 (u_x)^{s+1}_{1,M+1}. \tag{24}$$

The first derivative in Eq. (24) is deduced from Padé relation (13), i.e.,

$$-1 + (h/2)(u_x)^{s+1}_{1,M+1} + (h^2/12)(u_{xx})^{s+1}_{1,M+1} = 0.$$

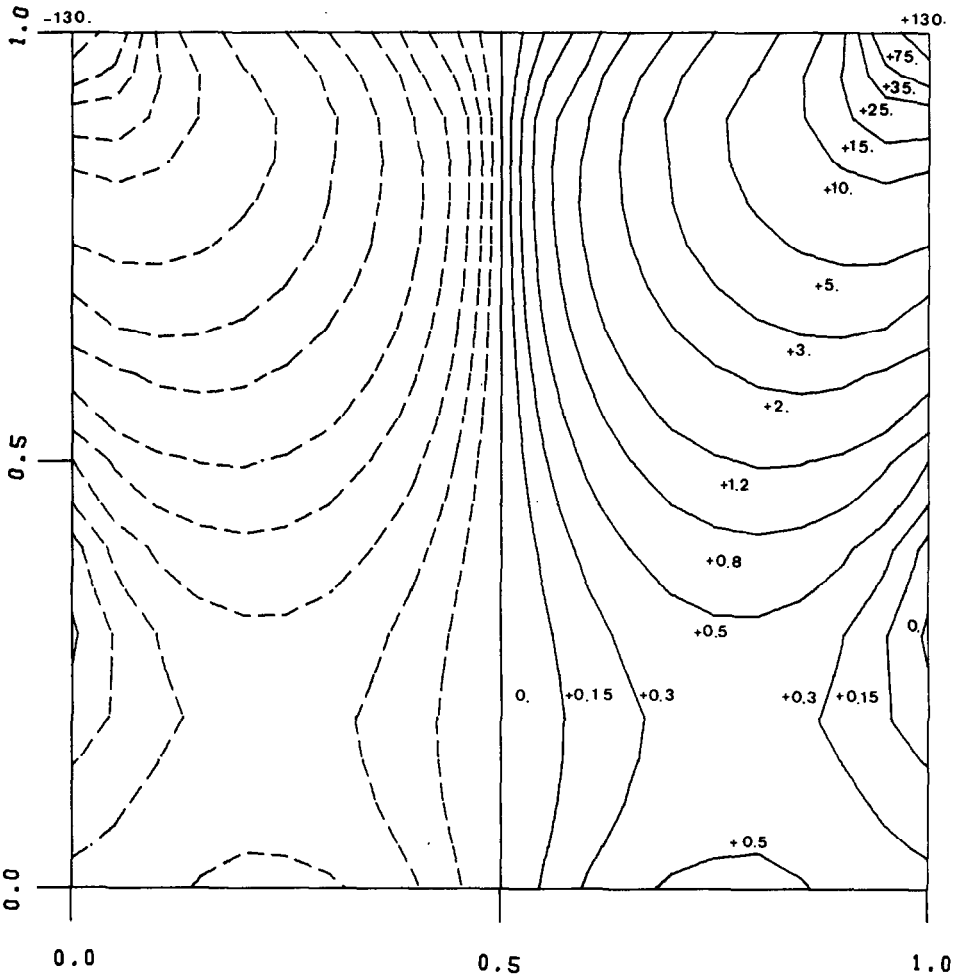

FIG. 7a. Contour lines of pressure for the square cavity problem; Re = 0 (Stokes flow).

The corner second-order derivative in the last equation is derived from the x-momentum equation,

$$(u_{xx})^{s+1}_{1,M+1} = \mathrm{Re}(p_x)^s_{1,M+1}.$$

The converged solution yields $u_x = 0$ at the two upper corners and at every point of Γ_4, and the second-order derivative u_{xx} of the viscous forces is in equilibrium with the pressure forces provided by p_x at the singularities.

With this special treatment at the singular corners, all the numerical results produced by the present method were obtained till the maximum divergence in absolute value was less than 10^{-5} and the pressure fields exhibit no oscillations. See Figs. 7a and b for pressure contour lines at $\mathrm{Re} = 0$ and 100, respectively, where $\mathrm{Re} = 1/\nu$, for a 21×21 grid.

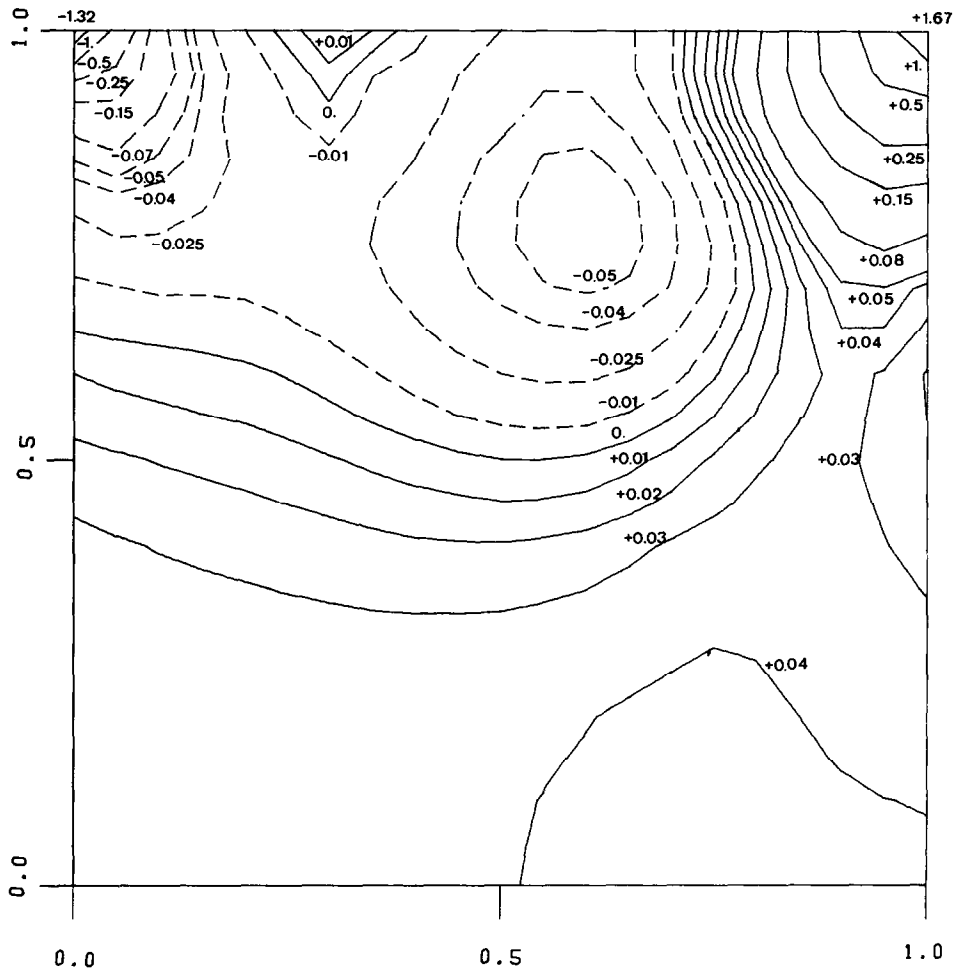

FIG. 7b. Contour lines of pressure for the square cavity problem; $\mathrm{Re} = 100$.

TABLE IV

Horizontal Velocity Component at $x = 0.1$, 0.5 (Re = 0) by Fourth-Order Compact Differences and Finite Element Method for the Square Cavity Problem ($N = 20$)

y	Present Authors $x = 0.5$	[13] $x = 0.5$	[13] $x = 0.1$	Present Authors $x = 0.1$
0	0.0	0.0	0.0	0.0
0.1	−0.05783	−0.05763	−0.00504	−0.00513
0.2	−0.1022	−0.1017	−0.0114	−0.0115
0.3	−0.1426	−0.1418	−0.0174	−0.0177
0.4	−0.1798	−0.1787	−0.0241	−0.0244
0.5	−0.2051	−0.2037	−0.0320	−0.0325
0.6	−0.1967	−0.1953	−0.0418	−0.0429
0.7	−0.1159	−0.1146	−0.0535	−0.0574
0.8	0.0903	0.0915	−0.0377	−0.0767
0.9	0.4655	0.4671	−0.00448	−0.0327
1.0	1.0	1.0	1.0	1.0

For Re = 0, Table IV compares the fourth-order calculation with a finite element technique due to Crochet [13]. This finite element code integrates the Navier–Stokes equations within the velocity-pressure formulation through a displacement method using 9-nodes Lagrangian elements. Inside the elements, the velocity and pressure are represented by biquadratic and bilinear approximations, respectively. At the singular corners, the quadrilaterals are degenerated into triangles by superposition of two vertices. This procedure allows an elegant treatment of corner discontinuities. Both methods have used a 20×20 grid. One notices that on the vertical centerline, both computations agree to two decimal places. At $x = 0.1$, the numerical results are close [illegible] the moving plate.

A similar behavior appears from the comparison of the results produced by the present method at Re = 1 and the computations by Piva *et al.* [14] using a finite element method with a nonorthogonal coordinates system.

We feel that the present fourth-order result is more accurate because reported fourth-order computations with the vorticity-stream function formulation (see Rubin and Khosla [15]) yield the same negative sign for the u velocity near the corner.

In order to demonstrate the real improvement acquired by the design of a judicious irregular mesh, Table V examines u values at two selected points ($x = y = 0.5$, $x = 0.1$ and $y = 0.9$) for Re = 0. One can see that for the 15×15 variable grid displayed in Fig. 8, the numerical values approach those computed on the finer grid with constant mesh. Notice that the variable grid is created in such a way that near the corners, the mesh size is close to $\frac{1}{20}$ while near the center point, the spatial step is $\frac{1}{10}$. One may therefore conclude that a discretization network with a smaller number of well distributed points can achieve the same level of accuracy as a finer grid with constant spatial step.

TABLE V

Horizontal Velocity Component at Two Selected Points for a Stokes Square Cavity Problem with Equally Spaced and Nonuniformly Distributed Mesh Points

N	Type of Mesh	$x = y = 0.5$	$x = 0.1, y = 0.9$
10	Constant	−0.2045	−0.0200
15	Variable	−0.2049	−0.0315
20	Constant	−0.2051	−0.0327

Moreover, to estimate the rate of convergence of the general algorithm on a two-dimensional problem presenting singularities, a convergence analysis has been performed on equipartitioned meshes for the square cavity problem with $N = M = 10$, 20, 30, 40, respectively. Nonetheless, as the singularities will influence the convergence order, this study treats simultaneously the standard problem and a regularized cavity [16], where a smooth u velocity component is prescribed on the top wall Γ_4, namely,

$$u(x, 1) = 16x^2(x-1)^2, \qquad 0 \leqslant x \leqslant 1.$$

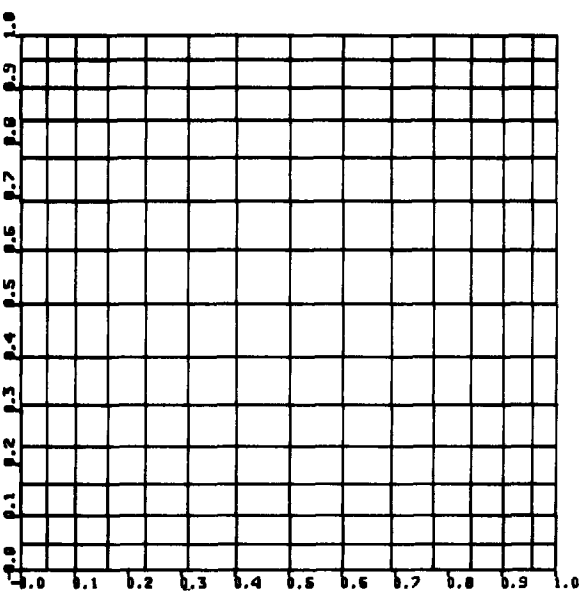

FIG. 8. A 15 × 15 variable grid for the square cavity problem.

TABLE VI

Global Rate of Convergence for u, v, and p, on the Standard and Regular Square Cavity Problems, for Re = 0, 100

	Re = 0		Re = 100	
Type of Problem	Reg	Std	Reg	Std
$n(u)$	3.80	3.15	3.82	3.20
$n(v)$	3.94	3.25	3.96	3.30
$n(p)$	3.05	2.20	3.04	2.20

The present analysis follows the guidelines of the numerical analysis by De Vahl Davis [17] on the benchmark solution of the thermal cavity problem.

The four used networks share an array of 11×11 points, which allows the comparison of u, v, p computed values at the same points.

The rate of convergence is first evaluated separately for u, v, and p from the numerical solutions obtained with $N = 10$, 20, 40 by the following formula (written for the u variable)

$$n(u) = \log(\| u_{20} - u_{10} \|_2 / \| u_{40} - u_{20} \|_2)/\log 2,$$

where n is the convergence order, u_i the u solution produced on a $i \times i$ grid and $\|f\|_2 = (\sum_{i,j=1}^{l} |f_{i,j}|^2)^{1/2}/l^2$ with l being the number of points where f is calculated. It should be noted that root mean square deviations between the various solutions appear in the previous relationship. This coherent procedure provides the global rate of convergence.

From this computed order of convergence, a reference solution is produced by an extrapolation procedure (e.g., for u)

$$u_{\text{ref}} = (2^{n(u)} u_{40} - u_{20})/(2^{n(u)} - 1).$$

Table VI summarizes the computed rates of convergence for u, v, and p at Re = 0 and 100 for both cavities.

As far as the regular problem is concerned, the rate of convergence is four and three, for the velocities and the pressure, respectively. The loss of one order of magnitude for the pressure field is typical of the numerical integration of the Navier–Stokes equations. On the standard problem, the same phenomenon occurs, but the singularities affect the global convergence and cause a drop of the rate of convergence by almost an order of magnitude. Figures 9a and b are logarithmic diagrams of u and p L_2 errors, respectively for Re = 0 and 100. From the comparison of both problems, one observes higher error levels on the standard cavity with respect to the regular one.

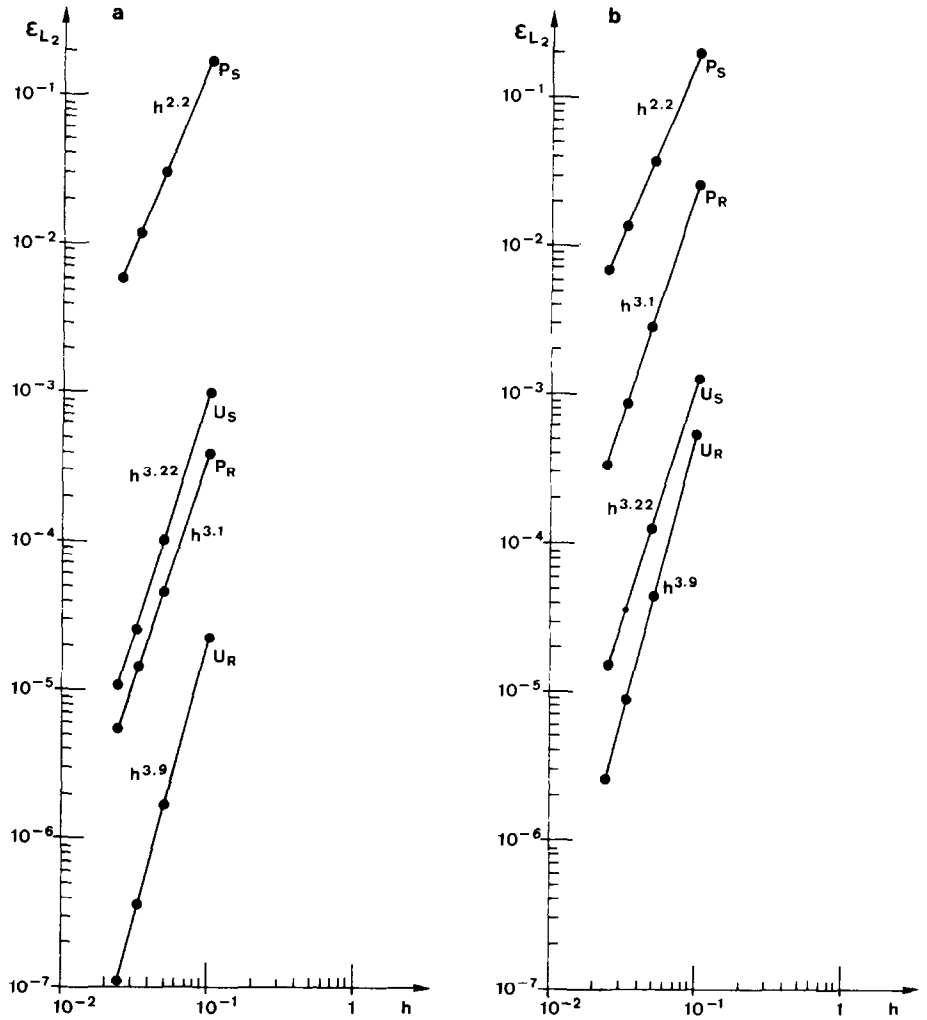

FIG. 9. Log–log error plot for the square cavity problem. (a) u and p error plot for the standard problem (U_S, P_S) and for the regular problem (U_R, P_R), at $\mathrm{Re} = 0$; (b) u and p error plot for the standard problem (U_S, P_S) and the regular problem (U_R, P_R) at $\mathrm{Re} = 100$.

Table VII gathers u values at the cavity center for the four grids and the pointwise rate of convergence. A typical running time on an IBM computer 370/158 is 5 sec/iteration for an $N = M = 20$ cavity; 65 iterations are needed for convergence at $\mathrm{Re} = 0$ while 135 iterations are necessary at $\mathrm{Re} = 100$, if the convergence criterion requires $|\max_{i,j} \mathrm{div}(\mathbf{v})_{i,j}| \leqslant 10^{-4}$.

We may conclude that the particular treatment of the boundary conditions has

TABLE VII

Values of the u Velocity Component at the Cavity Center for the Standard and Regular Cavity Problem for Various Grids

	Re = 0		Re = 100	
Type of Problem	Reg	Std	Reg	Std
N	U_{mid}	U_{mid}	U_{mid}	U_{mid}
10	−0.165681	−0.204308	−0.167411	−0.203516
20	−0.165487	−0.205068	−0.161573	−0.208576
30	−0.165477	−0.205131	−0.161310	−0.208972
40	−0.165475	−0.205149	−0.161242	−0.209076
$n(u)$	4.01	3.23	4.14	3.33
Extrap. Value	−0.1654744	−0.205161	−0.161220	−0.209147

Note. $n(u)$ is the pointwise rate of convergence. The last line provides u extrapolated values.

guaranteed a good rate of convergence and the use of a fourth-order method offers definite improvements over classical finite difference techniques, even for a problem with singularity.

6. Flow in a Plane Constricted Channel

Let us consider the flow in a plane channel presenting a cosine contraction (Fig. 10). This kind of domain was treated in Cheng [18] by a finite element method. The channel presents a longitudinal symmetry axis. The boundary is divided into three parts whose respective lengths are l_1, 1, l_2. Each boundary section is described by the functions

$$\begin{aligned} y(x) &= \pm 1, && 0 \leqslant x \leqslant l_1, \\ &= \pm 1 \mp \frac{\lambda}{2}\,[1 - \cos 2\pi(x - l_1)], && l_1 \leqslant x \leqslant l_1 + 1, \\ &= \pm 1, && l_1 + 1 \leqslant x \leqslant l_1 + l_2 + 1. \end{aligned}$$

The values of the λ parameter, which is the contraction parameter, are in between zero and one.

The Reynolds number in this case is defined as Re = flow rate/$\nu = 2/\nu$. The in- and outflow boundary conditions are the following:

(i) At the entry, a Poiseuille velocity profile is imposed by the equations

$$u = 1.5(1 - y^2), \qquad v = 0. \tag{25}$$

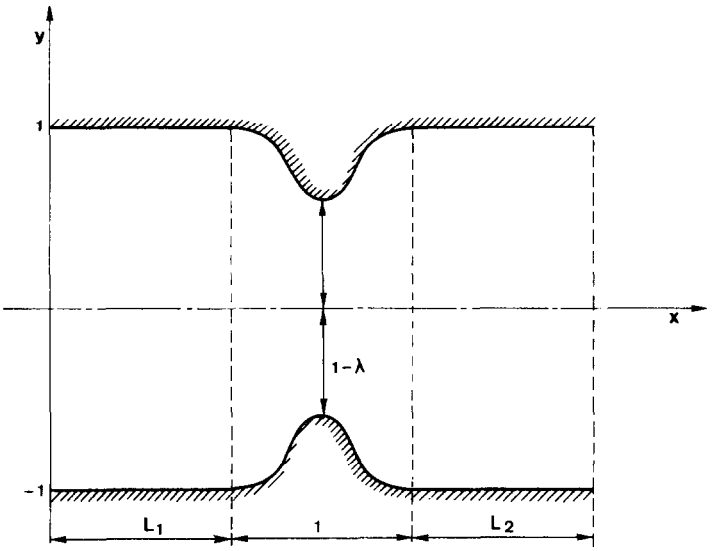

FIG. 10. Plane constricted channel.

The entry pressure comes from an artificial compressibility calculation by (4) that converges to $u_x = 0$.

(ii) At the outflow section, natural boundary conditions are imposed,

$$\text{vanishing normal stress: } T_n = -p + 2\mu u_x = 0, \tag{26a}$$

$$\text{Poiseuille shear stress: } T_s = \mu(v_x + u_y) = -3\mu y, \tag{26b}$$

where μ is the dynamic viscosity.

The outflow velocity components are obtained by Eqs. (21a), (21b). Equation (26a) provides the outflow pressure. Note that this procedure provides a vanishing reference pressure at node $(N+1, 1)$ on the fixed wall. The artificial compressibility scheme is not applied to the outflow section where, in fact, the equation $v_y = -u_x$ ensures the incompressibility.

Nonetheless, at moderate Reynolds numbers ($\mathrm{Re} \leqslant 100$), the following outflow boundary conditions may be set up:

$$v = u_x = p = 0, \tag{27}$$

instead of Eqs. (26) and yield the same numerical results.

The numerical problem solves only the upper part of the flow field by symmetry consideration. The l_1 and l_2 lengths are chosen sufficiently long to allow a reasonable development of the flow far away from the protuberance. Figure 11 shows a 16×8 discretization grid with $l_1 = 3.5$, $l_2 = 7.5$, $\lambda = 0.5$ for a $\mathrm{Re} = 50$ calculation. For

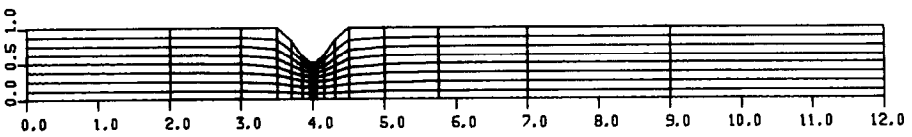

FIG. 11. Discretization grid for the plane constricted channel flow ($N = 16$, $M = 8$, $l_1 = 3.5$, $l_2 = 7.5$, $\lambda = 0.5$), with unevenly distributed cross sections and attraction near the protuberance.

Stokes flow ($\mathrm{Re} = 0$), $l_1 = l_2 = 4.5$ were chosen. It should be noted that in the boundary-fitted coordinate system computation, the constraint $x_\eta(\xi, \eta) \equiv 0$ leads to the generation of $\xi = \text{constant}$ lines which are orthogonal to the symmetry axis. Furthermore, it is taken full advantage of the flexibility of the geometric transformation method in order to space irregularly the successive cross sections: the first mesh size is two near the entry while the space step is 0.05 at the maximum contraction place where the flow undergoes important gradients. On the symmetry axis, boundary conditions are

$$v = 0, \qquad \frac{\partial u}{\partial y} = 0.$$

For Stokes flow ($\mathrm{Re} = 0$), three cases were computed, namely, $\lambda = 0$, 0.25, 0.5, over a 16×8 grid. The $\lambda = 0$ case yields the analytical solution of plane Poiseuille flow, with an absolute error on u, v, and p less than 10^{-5}.

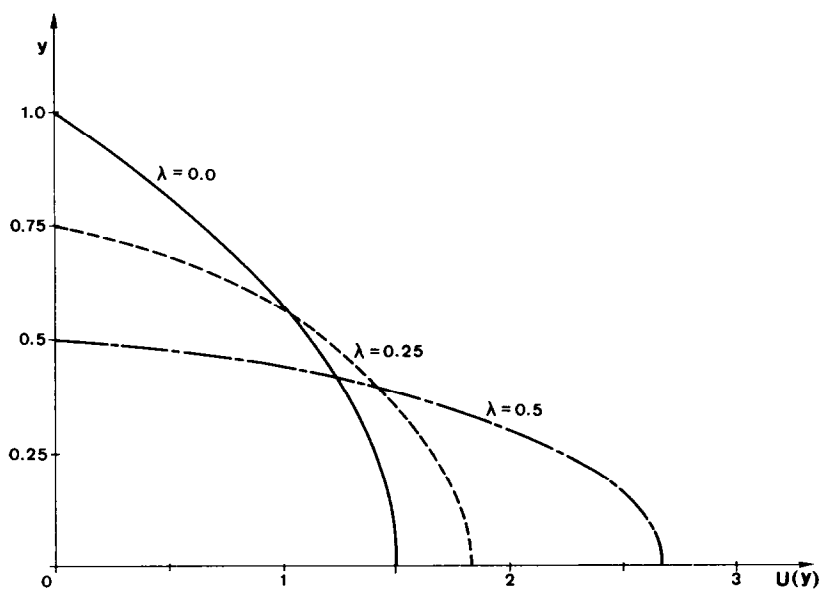

FIG. 12. Horizontal velocity component in the middle cross section; $\mathrm{Re} = 0$ (Stokes flow).

In Fig. 12, one observes the evolution of the horizontal u velocity component in the middle section, for various λ values. Figure 13 shows the pressure change on the longitudinal symmetry axis for increasing λ values. Note that the pressure gradients near the in- and outflow sections are constant. This indicates that the l_1 and l_2 lengths provide a good flow development.

For viscous flows at $\mathrm{Re} = 50$, with $\lambda = 0.5$, a recirculation zone appears behind the protuberance and a strong pressure gradient develops upstream of the constriction. Figure 14 displays u-velocity contours, where a windowing has been made in the vicinity of the contraction. One may notice the acceleration of the fluid near the top of the constriction, while, behind the protuberance, a recirculating flow is set up into motion. Further in the channel, the flow recovers the Poiseuille profile. Figure 15a shows the pressure field in the whole domain and Fig. 15b presents details through the same window as before.

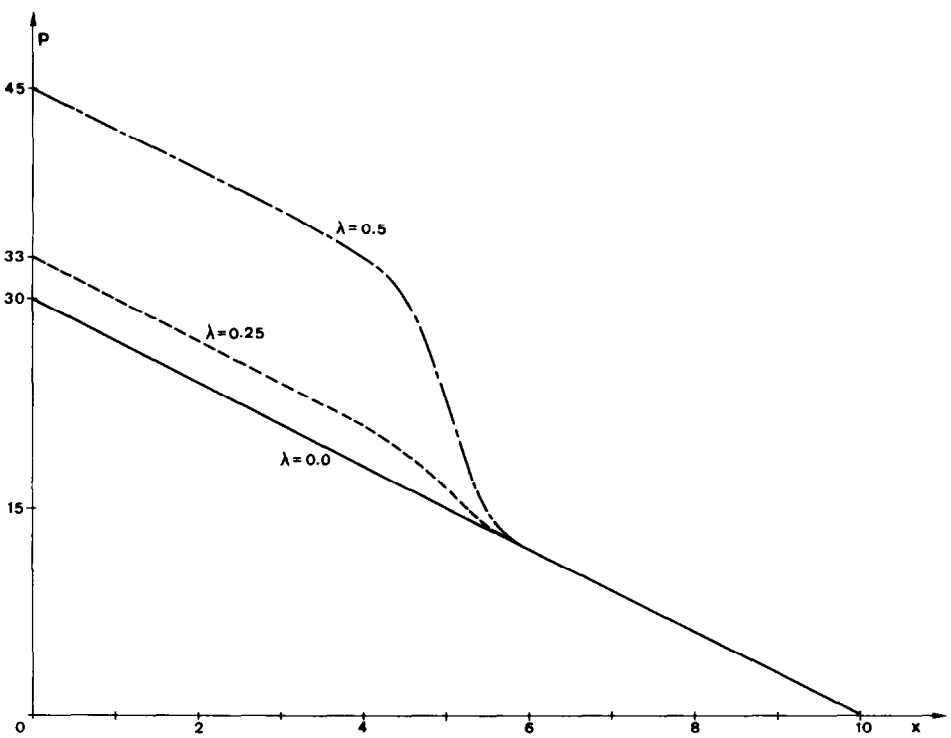

FIG. 13. Pressure distribution along the longitudinal symmetry axis; $\mathrm{Re} = 0$ (Stokes flow).

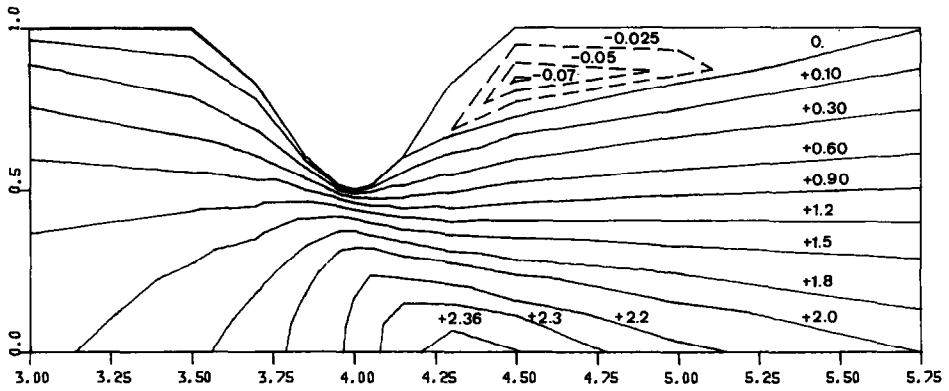

FIG. 14. Contour lines of the horizontal velocity component (u) near the constriction ($\lambda = 0.5$, $\mathrm{Re} = 50$).

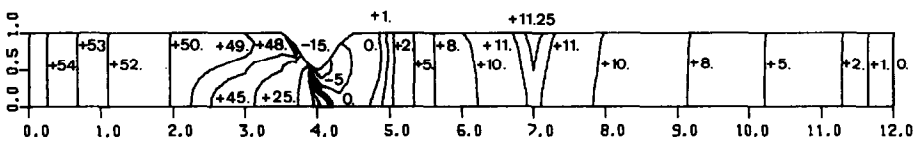

FIG. 15a. Contour lines of pressure ($\lambda = 0.5$, $\mathrm{Re} = 50$); global view.

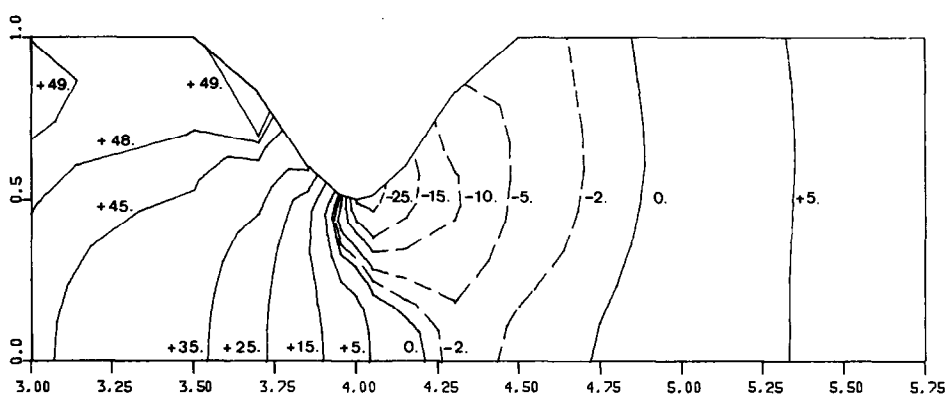

FIG. 15b. Contour lines of pressure ($\lambda = 0.5$, $\mathrm{Re} = 50$); window in the protuberance vicinity. (The pressure values are multiplied by 25 in Fig. 15a and 15b.)

CONCLUSIONS

We have investigated steady viscous flows by using fourth-order compact differences coupled with Thompson's transformation inside the velocity-pressure framework. Discretized quantities are attached at the same nodes. On a Stokes test problem, we show that discretization of pressure and velocity at the same grid points leads to meaningful results because of the implicit character and the improved accuracy of the fourth-order formulation. Furthermore, the boundary-fitted coordinates provide the user with a powerful tool to improve by several orders of magnitude the accuracy in regions of interest.

Standard numerical problems as Poiseuille, Couette flow, and the square cavity are solved. The numerical results compare favourably with other numerical techniques. The flexibility of irregular grid generation is emphasized.

A convergence analysis carried out on the standard cavity problem reveals a loss by about an order of magnitude for the velocity and pressure rates of convergence with respect to those obtained for the smooth cavity, where they are of order four and three, respectively.

The final test consists in the evolution of a plane constricted channel flow. This last problem shows that the application of finite differencing with a mapping technique to the treatment of a geometrically complex flow region falls within the realm of feasibility.

APPENDIX: THE TRANSFORMATION METHOD

The fundamental idea of Thompson's transformation [3] is the generation of transformed ξ and η functions such that each boundary of the physical domain $D(x, y)$ coïncides with a coordinate line (Fig. 1). This can be achieved by considering the ξ and η functions as the solutions of an elliptic partial differential problem, namely,

$$\xi_{xx} + \xi_{yy} = P(x, y), \tag{A1}$$

$$\eta_{xx} + \eta_{yy} = Q(x, y), \tag{A2}$$

where, for example ξ_{xx} denotes the $\partial^2\xi/\partial x^2$. In Eqs. (A1) and (A2), P and Q are given functions regulating the mesh interval inside the domain. The elliptic problem satisfies Dirichlet boundary conditions.

As the numerical integration is performed in the transformed plane, the role of dependent and independent variables is interchanged in (A1) and (A2). One gets the coupled system,

$$\alpha x_{\xi\xi} - 2\beta x_{\xi\eta} + \gamma x_{\eta\eta} + J^2(Px_\xi + Qx_\eta) = 0, \tag{A3}$$

$$\alpha y_{\xi\xi} - 2\beta y_{\xi\eta} + \gamma y_{\eta\eta} + J^2(Py_\xi + Qy_\eta) = 0, \tag{A4}$$

with

$$\alpha = x_\eta^2 + y_\eta^2, \qquad \beta = x_\xi x_\eta + y_\xi y_\eta, \qquad \gamma = x_\xi^2 + y_\xi^2, \qquad J = x_\xi y_\eta - x_\eta y_\xi. \tag{A5}$$

In Eqs. (A3)–(A5), J is the Jacobian of the transformation. It is assumed that J^{-1} exists and J does not vanish. If f denotes a sufficiently differentiable function defined on D, the partial differentials are changed to the next relationships,

$$f_x = (y_\eta f_\xi - y_\xi f_\eta)/J, \tag{A6a}$$

$$f_y = (-x_\eta f_\xi + x_\xi f_\eta)/J, \tag{A6b}$$

$$\nabla^2 f = (\alpha f_{\xi\xi} - 2\beta f_{\xi\eta} + \gamma f_{\eta\eta})/J^2 + P f_\xi + Q f_\eta. \tag{A6c}$$

Similar expressions hold for other derivatives and operators.

The one-dimensional natural coordinates, which are used in Section 3, are obtained by the 1-D version of Eq. (A3),

$$x_{\xi\xi} + (x_\xi)^3 P(\xi) = 0, \qquad 1 \leqslant \xi \leqslant N+1 \tag{A7}$$

with appropriate boundary conditions. Here, N is the number of intervals in the computational domain. The P function has the form,

$$P(\xi) = \sum_{i=1}^{N+1} a_i \operatorname{sgn}(\xi - \xi_i) \exp(-c_i |\xi - \xi_i|). \tag{A8}$$

In (A8), the a_i and c_i coefficients are, respectively, the positive amplitude and modification factors, which create controlled distortion of the network. The first- and second-order derivatives become, respectively,

$$f_x = f_\xi (x_\xi)^{-1}, \qquad f_{xx} = f_{\xi\xi}(x_\xi)^{-2} - f_\xi x_{\xi\xi}(x_\xi)^{-3}. \tag{A9}$$

ACKNOWLEDGMENTS

One of us (X. A.) gratefully acknowledges the I.R.S.I.A. (Institut pour l'encouragement de la Recherche Scientifique dans l'Industrie et l'Agriculture) which made this research possible through a specialization grant.

REFERENCES

1. F. H. HARLOW AND J. E. WELCH, *Phys. Fluids* **8** (1965), 2182.
2. B. D. NICHOLS AND C. W. HIRT, *J. Comput. Phys.* **8** (1971), 434.
3. J. F. THOMPSON, F. C. THAMES, AND C. W. MASTIN, *J. Comput. Phys.* **15** (1974), 299.
4. J. K. HODGE, "Numerical Solution of Incompressible Laminar Flow about Arbitrary Bodies in Body-fitted Coordinates," Ph.D. Thesis, Mississipi State University, 1975.

5. J. F. THOMPSON, *in* "Computational Fluid Dynamics," Lecture Series, No. 1978-4, Von Karman Institute for Fluid Dynamics, 1978.
6. A. J. CHORIN, *J. Comput. Phys.* **2** (1967), 12.
7. D. GOTTLIEB AND S. A. ORSZAG, *in* "CBMS–NSF Monograph Series," Vol. 26, SIAM, Philadelphia, 1977.
8. S. A. ORSZAG AND M. ISRAELI, *Ann. Rev. Fluid Mech.* **6** (1974), 281.
9. R. S. HIRSCH, *J. Comput. Phys.* **19** (1975), 90.
10. E. ISAACSON AND H. B. KELLER, "Analysis of Numerical Methods," Wiley, New York, 1966.
11. G. D. MALLINSON AND G. DE VAHL DAVIS, *J. Comput. Phys.* **12** (1973), 435.
12. E. ELSAESSER AND R. PEYRET, "Méthodes Hermitiennes pour la résolution numérique des Équations de Navier–Stokes," Comptes Rendus du Congrès International sur les Méthodes Numériques dans les Sciences de l'Ingénieur, Paris, 1978.
13. M. J. CROCHET, private communication.
14. R. PIVA, A. DI CARLO, AND G. GUJ, *Comput. Fluids* **8** (1980), 225.
15. S. G. RUBIN AND P. K. KHOSLA, "Higher-Order Numerical Methods Derived from Three-Point Polynomial Interpolation," NASA CR-2735, August 1976.
16. M. BOURCIER AND C. FRANÇOIS, "Numerical Integration of the Navier–Stokes Equations in a Square Domain," La Recherche Aérospatiale, Vol. 131, pp. 23–33, 1969.
17. G. DE VAHL DAVIS, "Natural Convection of Air in a Square Cavity: An Accurate Numerical Solution," Report 1981/FMT/1, University of New South Wales, School of Mech. and Indust. Eng., 1981.
18. R. T. CHENG, *Phys. Fluids* **15** (1972), 2098.